Electronic Supplementary Material (ESI) for Journal of Materials Chemistry C.
This journal is © The Royal Society of Chemistry 2021

Supplementary Figures

Heat diffusion of the local damage area

Heat diffusion of the local damage during single ion implantation process was investigated. The normal stresses of NCDS atoms (i.e., σ_{xx}, σ_{yy}, and σ_{zz}) were weighted and averaged before taking an absolute value. Figure 1 shows local average stress and average temperature evolution during thermal spike. It can be observed that the local temperature is close to 2000 K when damage cascade is maximized, inducing the self-annealing effect to eliminate part of the local damage. According to the repair rate of damaged atoms, the self-repair process can be divided into fast recovery stage and slow recovery stage, as shown in Figure 1. It can be assumed that the magnitude of velocity reflects the role of phonons in thermal peak effect, noticed that the average speed range of the amorphous atoms was consistent of ~1500 m/s to ~3000 m/s for both Elstop implantation and Elstop-off implantation during fast recovery, with the same time spent. However, the speed of damaged atoms decreased faster for Elstop implantation during slow recovery state with a speed range of ~1000 m/s to ~1500m/s, compared to the value of ~1200 m/s to ~1500m/s for Elstop-off implantation.

In addition, fast recovery phase of the Elstop implantation took less time than the Elstop-off implantation: as evident from Figure 1, the local stress decreased from ~19 GPa to ~14 GPa in 0.12 ps, and then it took 0.45 ps to reduce to 10 GPa. From a close survey of the literature [1], the local stress should be in the order of 10 GPa during thermal spike. As for Elstop-off implantation, the fast recovery phase decreased from ~23 GPa to 15 GPa in the same time as 0.12 ps, and slow recovery took 0.56 ps to decrease to 10 GPa. Then, stress was released quickly through phonon propagation, which caused some damaged atoms returning to normal lattice position. Finally, the stress of damage area in both cases was stabilized at 5 GPa in the damage stable state.

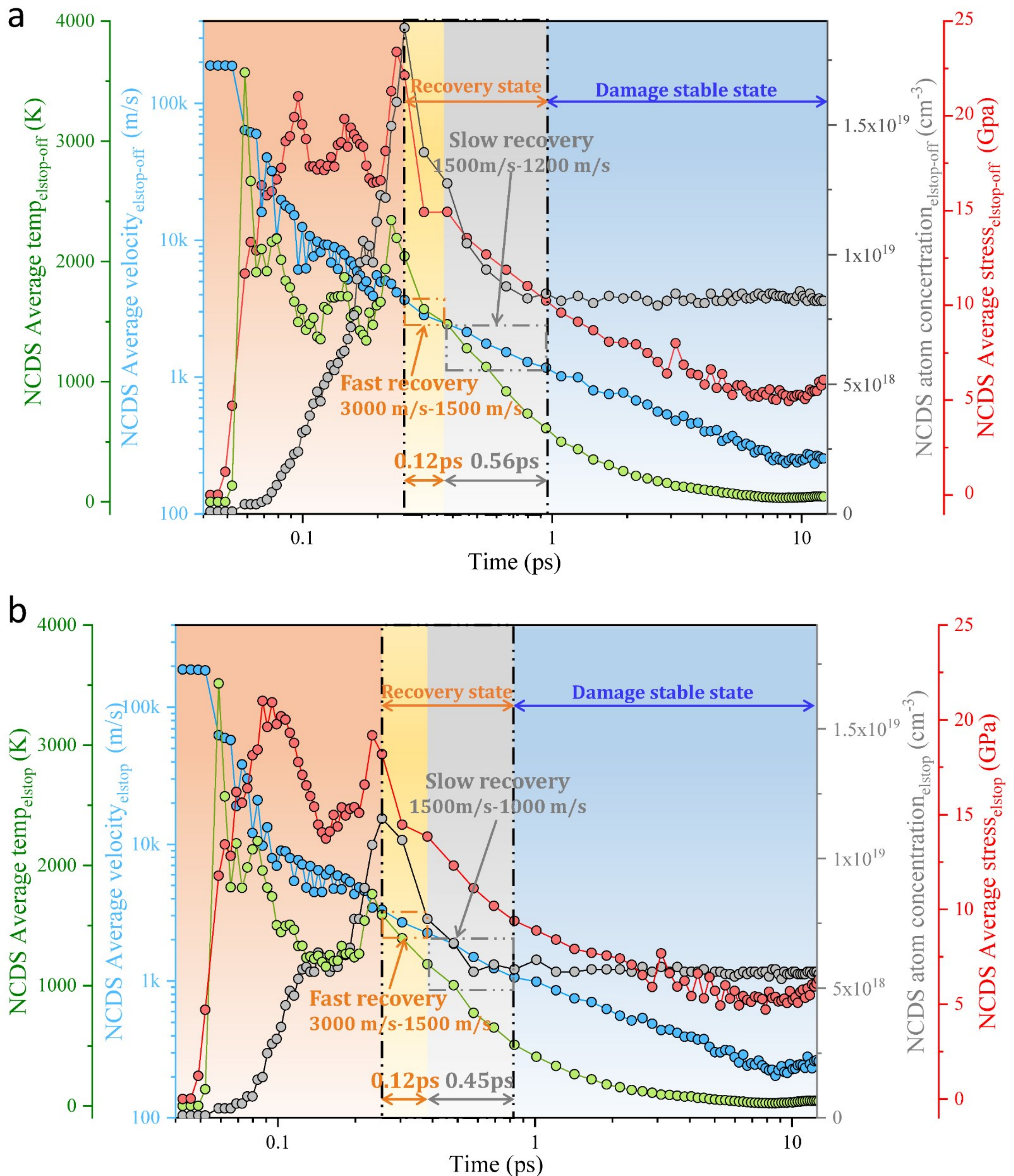

Supplementary Figure 1. Evolution of average temperature, velocity and stress of damaged area during thermal spike, obtained from (**a**) Elstop-off implantation and (**b**) Elstop implantation. The black dashed box represents the recovery stage of damage. Due to the extremely short occurrence time of the whole process, a logarithmic transformation to the abscissa of 12 ps was used.

Classical thermal spike model

Under keV irradiation conditions, nuclear stopping (momentum transfer) was usually dominant in local damage formation. When considering the electronic energy transfer, these two primary energy transfers were entangled with equilibrium heating and non-equilibrium excitation processes [2]. We performed thermal decomposition for the 5 keV single ion implantation. The resulting thermal spike is shown in Figure 2. Combining the above-mentioned average temperature and damage evolution of damaged atoms, it can be seen that the cascade collision effect makes the local temperature very high at a quarter picosecond, the temperature drops rapidly with the radial distance from the ion. In the selected case, the maximum diameter with a temperature exceeding 1000 K was roughly 1.5 nm, which is about the order of the radius of a typical experimental orbit [3].

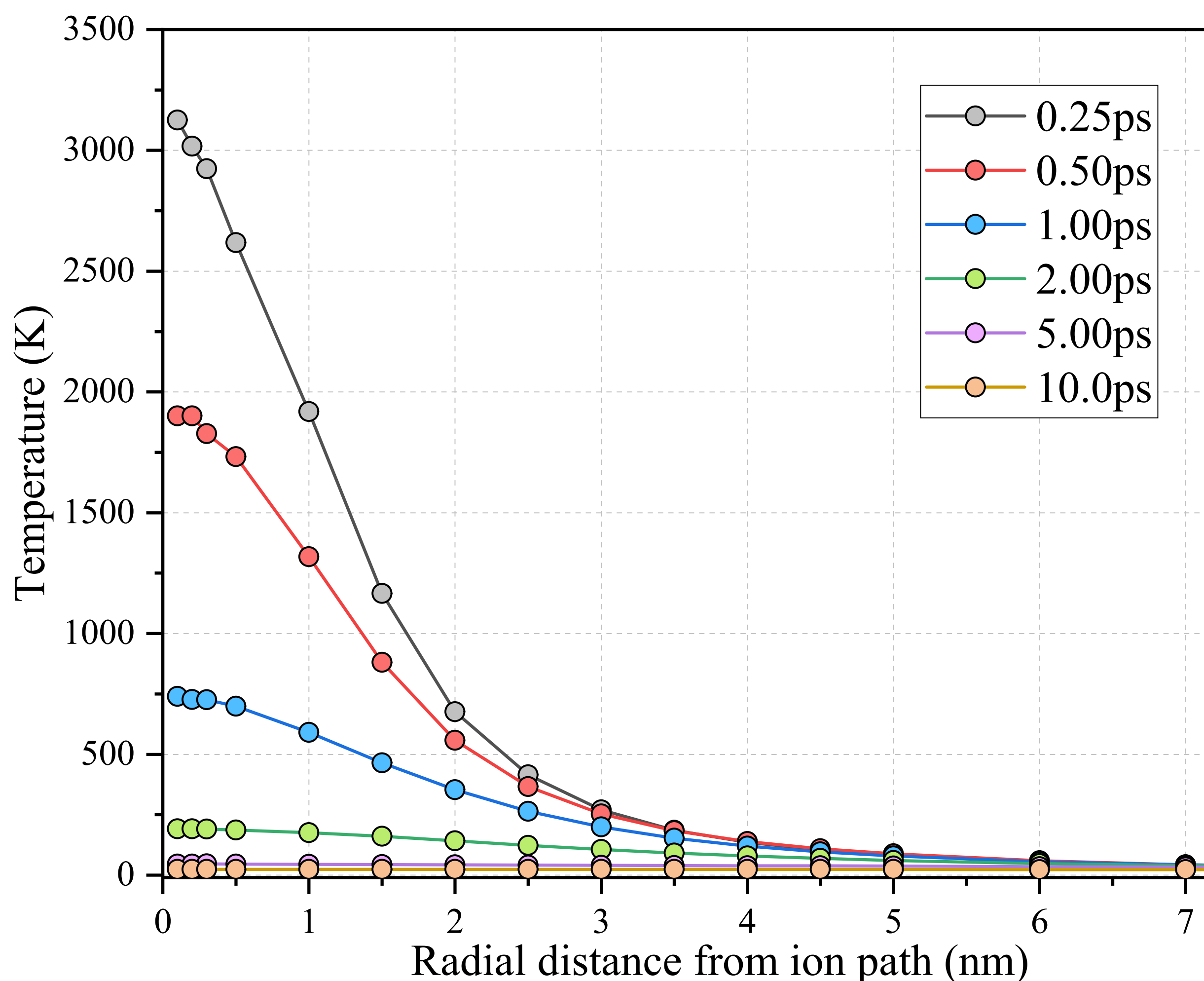

Supplementary Figure 2. Time-space evolution of thermal spike considering ionization calculated by spherical calculation with a cutoff radius of 1 nm. The radial and temporal evolution of 3C-SiC system temperature for 5 keV Al single-ion at 0 K. With increasing time the temperature maximum decreases rapidly.

The limitation of WS analysis during HT dynamic simulations

The volume of the workpiece fluctuates due to drastic changes in temperature during annealing. Figure 3 shows a snapshot of 3300 K annealing process for the test model (implantation at the dose of 1.25 × 10^{14} cm^{-2} mentioned in section 2.2), specifically the distribution of interstitials identified by WS analysis and colored by IDS, at a certain time in heating insulation stage (where non-interstitials were hidden). A part of perfect CDS "interstitials" was randomly selected for magnification, as shown in Figure 3. It can be seen that this part completely conforms to the supercell structure of 3C-SiC, and there are no interstitials around the atoms in lattice sites. Therefore, we conclude that it is unreasonable to use the WS analysis as a basis to judge the existence of interstitials in heating-related simulation, i.e., the WS method is not perfectly suitable for ion implantation and high temperature (HT) annealing process.

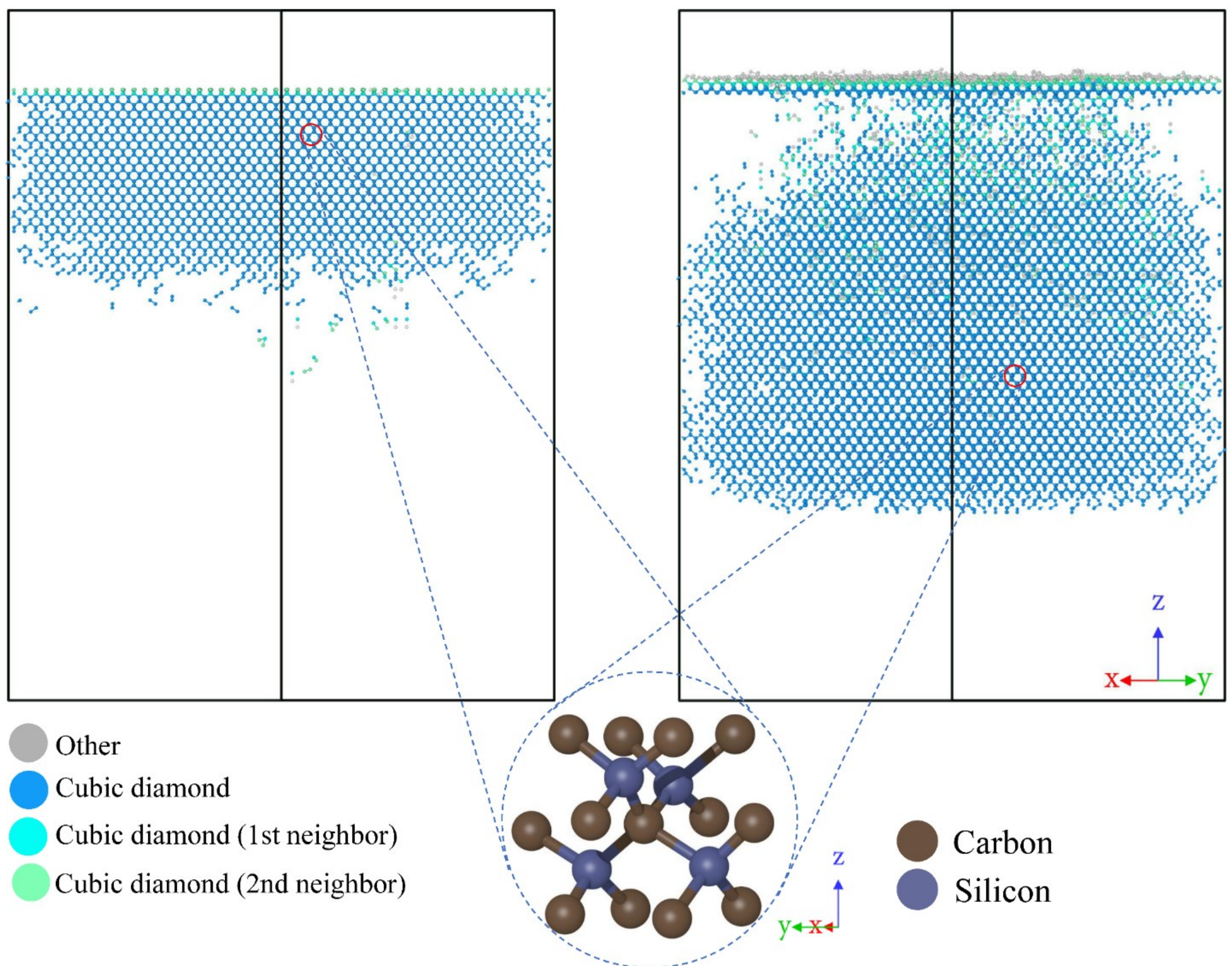

Supplementary Figure 3. The distribution of interstitial atoms (colored by IDS) and local detail of "interstitials" calculated by WS analysis in perfect CDS during the first ion implantation (left figure), and during 3300 K annealing process (right figure).

The choice of temperature for HT implantation and annealing

We chose 873 K and 1273 K as standard temperature for HT implantation. Moreover, a higher implantation temperature i.e. 1973 K was chosen, purely to observe the influence of temperature on the evolution of damage.

As for the annealing temperature, the annealing temperature range of 3200 ~ 3700 K is initially determined according to the calculated T_D (4740.8 K). Since the main focus in this study is on the exploration of NCDS atoms and doping efficiency after RT or HT implantation and subsequent equal-condition annealing, so a certain annealing temperature should be further determined. The temperature from 3100 K to 3500 K was divided into five parts with the same annealing process (the rate of heating and cooling was 2×10^{13} K / s, the heating state was holding for 2 ns, and the relaxation equilibrium after cooling to RT was kept for 0.05 ns). As shown in Figure 4, HT annealing at 3300 K corresponds to the lowest damage atom concentration and the highest doping efficiency. Noted that the HT annealing at 3400 K and 3500 K makes the NCDS atom concentration increase sharply, which indicates that an excessive high annealing temperature will instead lead to a decrease of recrystallization quality. In view of this, we determine to choose the annealing temperature of 3300 K for this study.

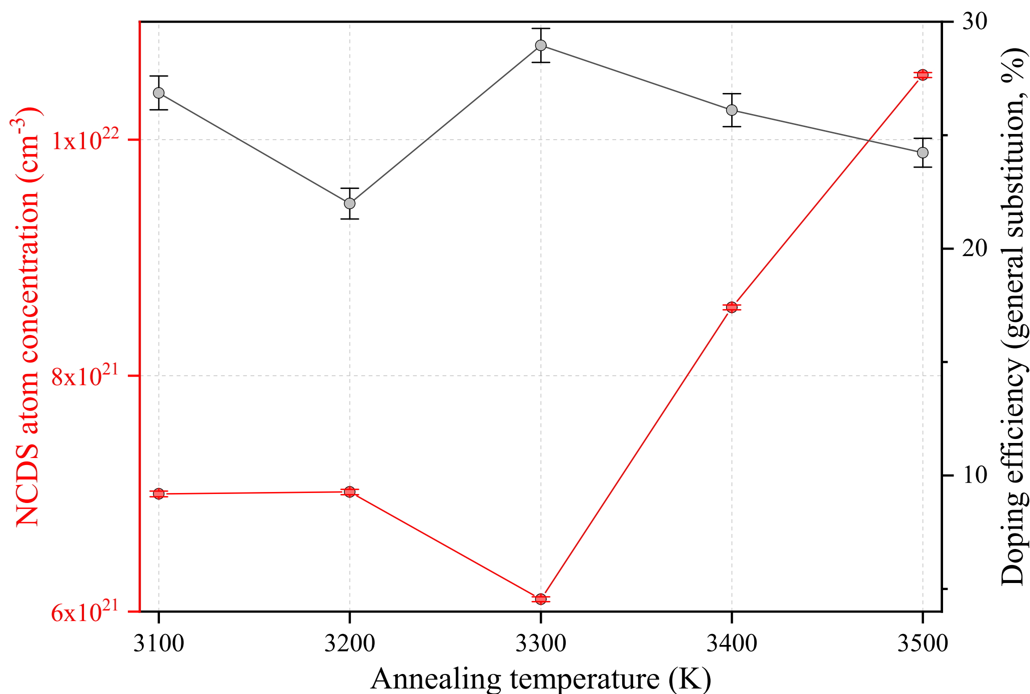

Supplementary Figure 4. The variation of NCDS atom concentration and doping efficiency under different annealing temperatures. The models used in five annealing cases are all RT implantation with the dose of 5×10^{14} cm^{-2}.

Determine the definition of “doping efficiency” in MD simulation

According to the first-principles calculation results performed by Wang et al. [4], the difference for the $Al_{Si}V_C$ band structure between 4H-SiC and 3C-SiC is that, the defect levels of $Al_{Si}V_C$ shows singlet levels in the band gap for a 4H-SiC crystal, while such defect levels are about 0.51 eV above the conduction bands minimum (CBM). The common feature is that the $Al_{Si}V_C$ all embody the characteristics of donors, which is in contrast to the acceptor role of Al_{Si}. Here we take the focus on the full band structure of substitutional Al with a carbon divacancy around it (Al_{Si}-diV_C), to determine whether the defective structure of substitutional Al with more than one V_C around will introduce defect levels in the band gap, or just lie in the conduction band region. In the energy calculations, the generalized gradient approximation (GGA) in the form of Perdew, Burke, and Ernzerhof (PBE) [5] was used for the exchange-correlation functional. The electronic band structures of perfect 3C-SiC lattice and Al_{Si}-diV_C in a 4 × 4 × 4 supercell are shown in Figure 5. Although PBE calculation underestimates the band gap, it still gives defects levels under the CBM (Figure 5b), which reflects a more serious donor role as $Al_{Si}V_C$ acts. Hence, the vacancies around substitutional Al may be responsible for the inhibition of hole in the valence band for Al-doped SiC.

As discussion above, we divided the “doping efficiency” into “perfect substitution” case and “general substitution” case, respectively (see section 2.4). The evolution trends of two substitution conditions under different temperature implantation with subsequent equal-conditions annealing were performed. The results are shown in section 3.3.

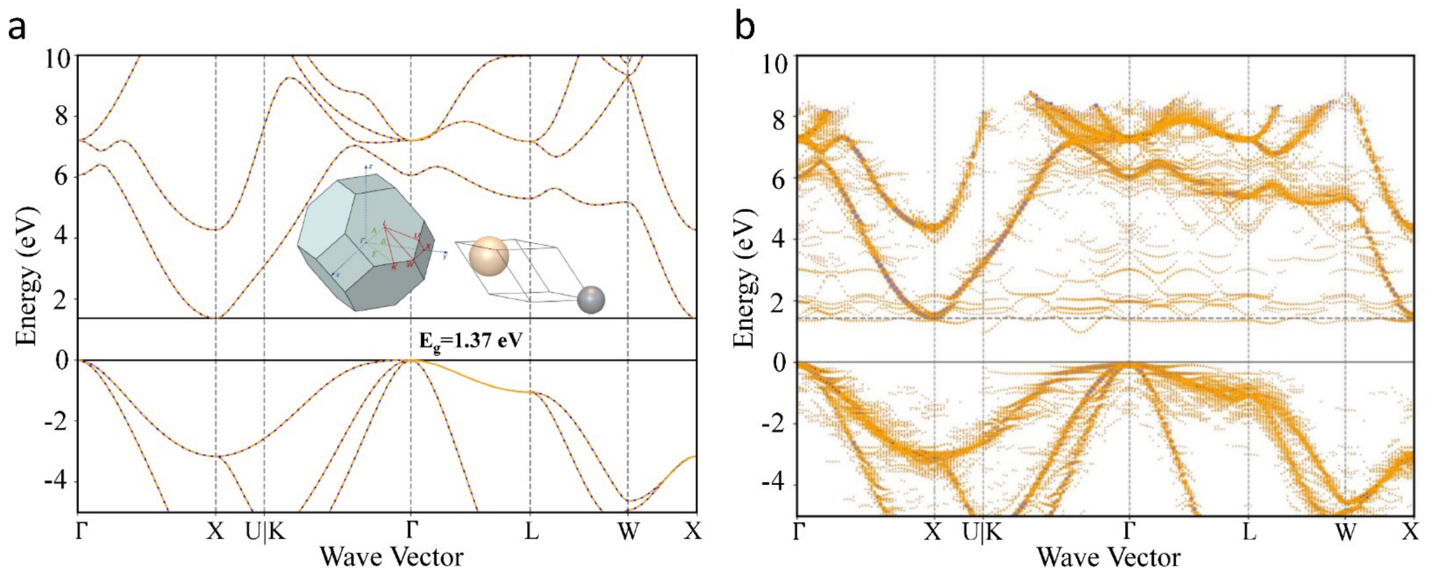

Supplementary Figure 5. Electronic band structures of (**a**) perfect 3C-SiC lattice, (**b**) complex defect where two carbon vacancies around Al center. Note that a limitation of the theoretical calculation leads the absolute values of the band gap (E_g) are underestimated.

The depth distribution of NCDS atoms before and after annealing

In Figure 6 we compare the depth distribution of NCDS atoms before and after 2.35 ns annealing at 3300 K. Noted that a more damage is caused by RT implantation than HT implantation (see Fig. 20 of the text). Therefore, according to Fig. 6 (a), the depth of the implantation region can be determined as 9 nm (the same depth was selected for HT implantation to count the evolution of NCDS atom concentration). According to this definition, the NCDS atom density in implantation area can be obtained intuitively. In other words, the degree of amorphization of the implanted area can be directly reflected by the NCDS atom density (the atomic density of crystal material is 9.72×10^{22} cm^{-3} as a reference). As mentioned before, the surface atoms can be regarded as boundary atoms with broken bonds so that it is easy to form surface atoms migration at HT conditions. Kimoto pointed out that the main driving force for surface migration is minimization of the surface energy of the crystal [6]. Evidence for this is in Figure 6 that the concentration of NCDS atoms close to surface layer was higher than the internal ones after HT annealing, while the internal damage was repaired significantly. Another remarkable phenomenon was that the peak damage concentration tended to approach the free surface of the workpiece as dose increased to 5×10^{14} cm^{-2}. There are two possible reasons for the above: firstly, NCDS atoms have a tendency to migrate to free surface during HT annealing; secondly, recrystallization occurs preferentially at the interface between NCDS atoms and crystal atoms and grows along the interface to the surface. This is supported by recent publications. For instance, in the study of annealing kinetics of gallium ion milling of single crystal silicon, Xiao et al. [7] pointed out that annealing is a process of re-growth of crystalline silicon from bottom to top surface and from periphery towards center. However, this cannot explain the observed "right shift" of the damage peak towards larger depths for doses below 4.06×10^{14} cm^{-2}. In view of this, we explored the recrystallization process of atoms during annealing.

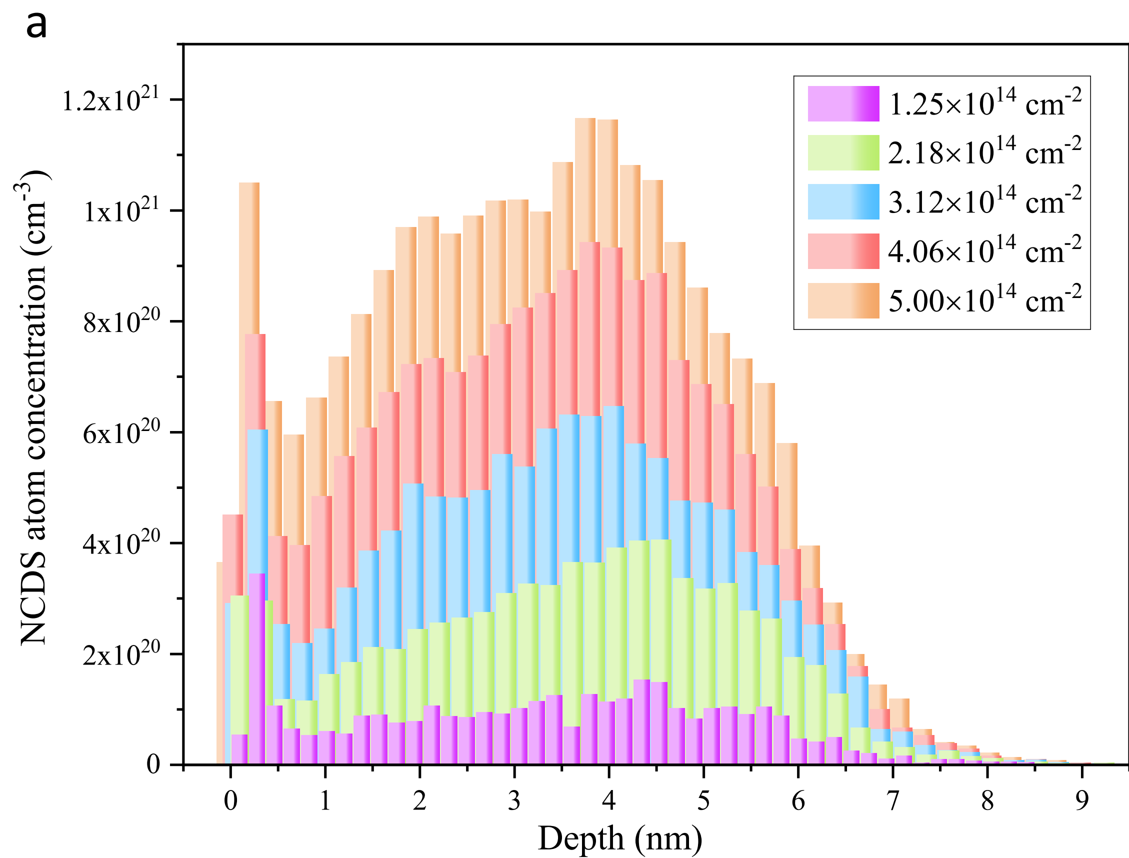

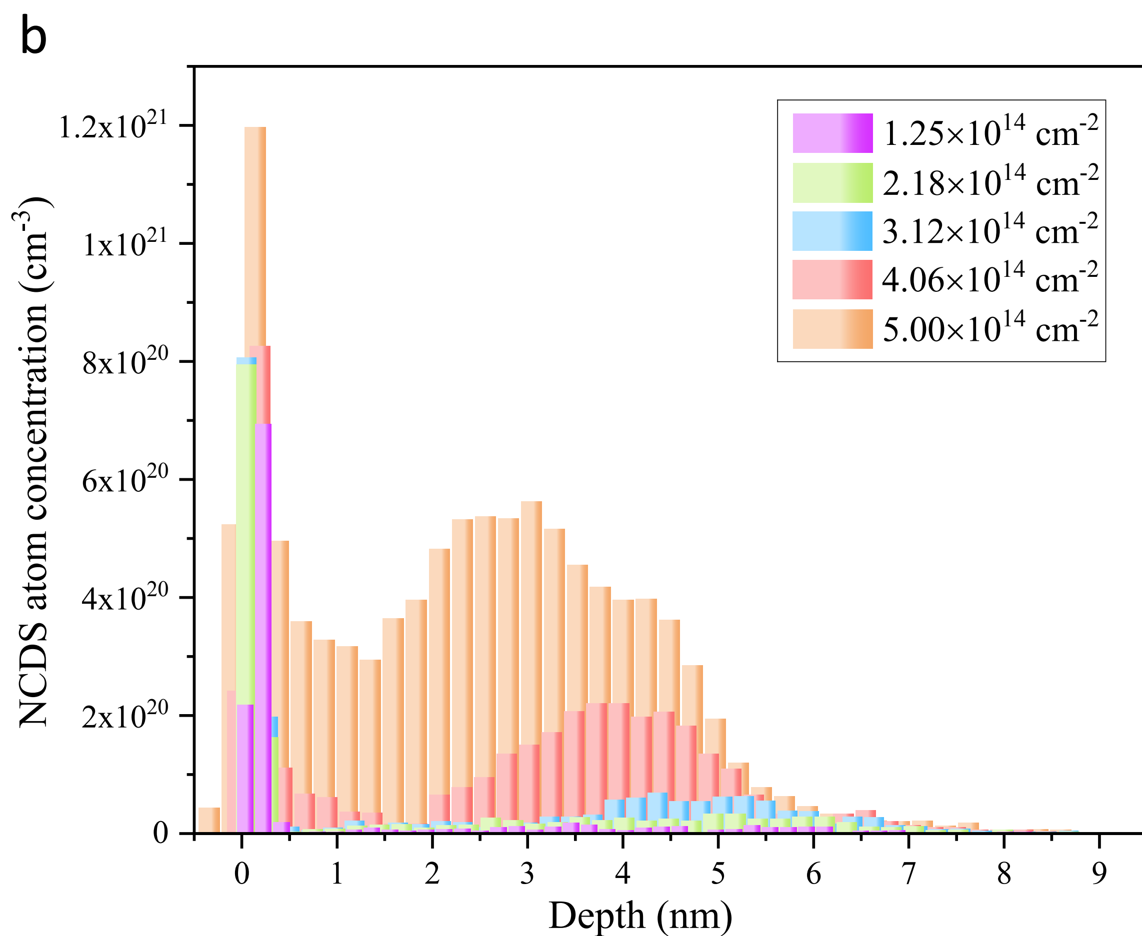

Supplementary Figure 6. The distribution of NCDS atom concentration under different implantation doses (**a**) after RT implantation, before and (**b**) after 2.3 ns annealing at 3300 K.

Stress distribution of annealed model after HT implantation

Due to the failure to form a closed crystal surface after post RT implantation annealing at the dose of 5×10^{14} cm^{-2} (as section 3.2 discussed), the stress distributions of post HT implantation annealing (under the same conditions i.e., 2.35 ns, 3300 K) in this certain dose were shown in Figure 7. As we expected, the crystal surface was closed after crystallization process due to a less damage formation during HT implantation than RT implantation (noted that the post 873 K implantation annealing still fails to form a closed crystal surface). The inset in Figure 7 quantifies the average compressive stress variation, which also confirms the conclusion mentioned in section 3.2, i.e. when the crystal surface was closed (as shown by the post 1273 K and 1973 K implantation annealing results), the residual defects in the lattice will cause a more concentrated compressive stress than that of post RT implantation annealing. In addition, no dislocation was formed at all the investigated doses after HT-implantation annealing.

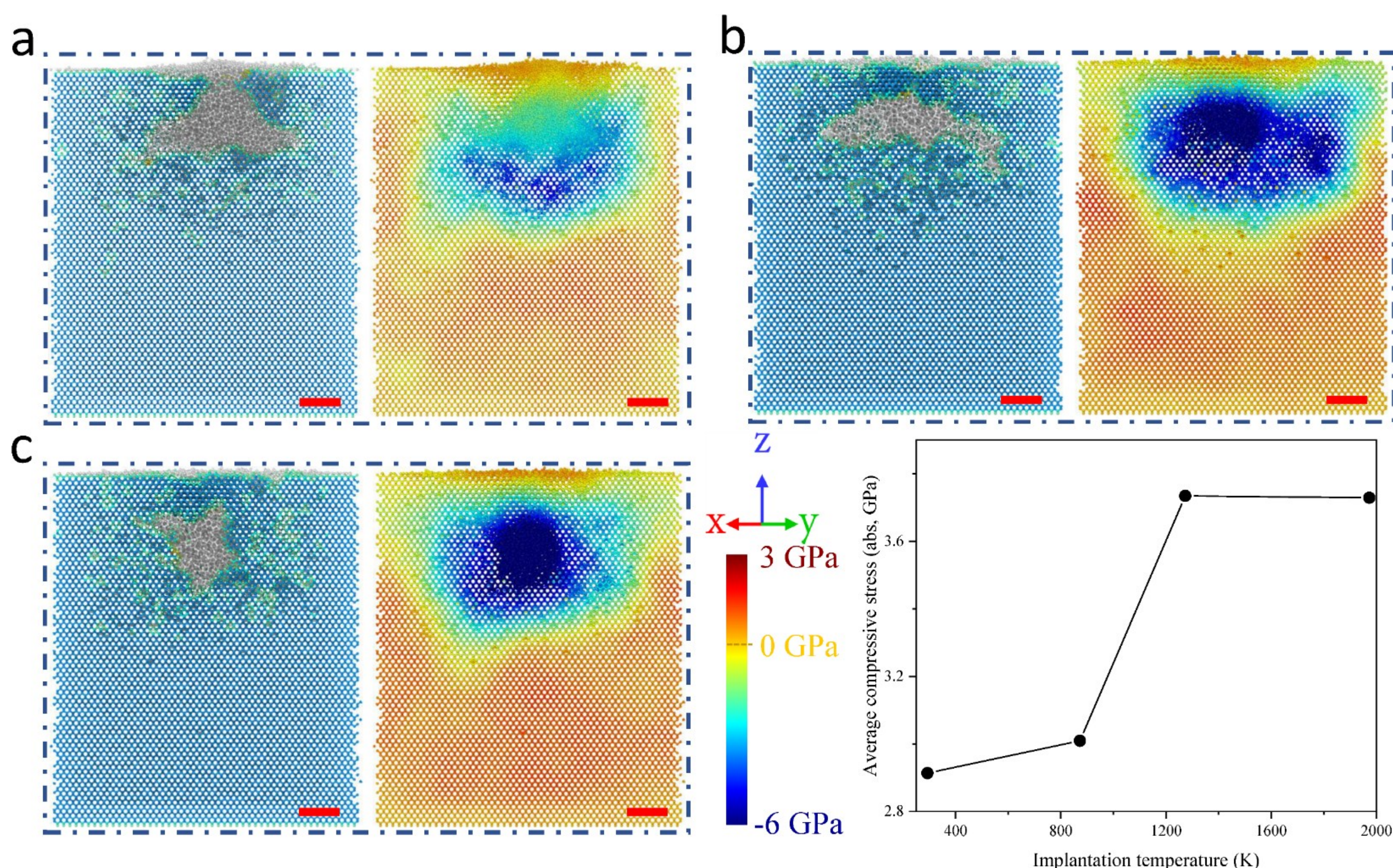

Supplementary Figure 7. Atomic structure and stress distribution of cross-sectional (110) view after 3300 K, 2.35 ns annealing, implant dose: 5×10^{14} cm^{-2}. (**a**) post 873 K implantation annealing, (**b**) post 1273 K implantation annealing, and (**c**) post 1973 K implantation annealing. Scale bar = 2 nm. The inset represents the average compressive stress (absolute value) after post RT and HT implantation annealing.

Inverse mapping method to uncover the annealing-induced defects

Figure 8 shows the “inverse mapping method” to identify the annealing-induced defects in SiC before and after annealing. By extracting the atoms inside the lattice at the final moment, these certain atoms were "frozen", then inverted to the moments before annealing (after implantation). The CDS atoms before annealing shown in Figure 8 represent the NCDS atoms formed by annealing. Due to the smaller threshold displacement energy of C, it is easier to form vacancies or other defects under heating excitation, including related deep level defects.

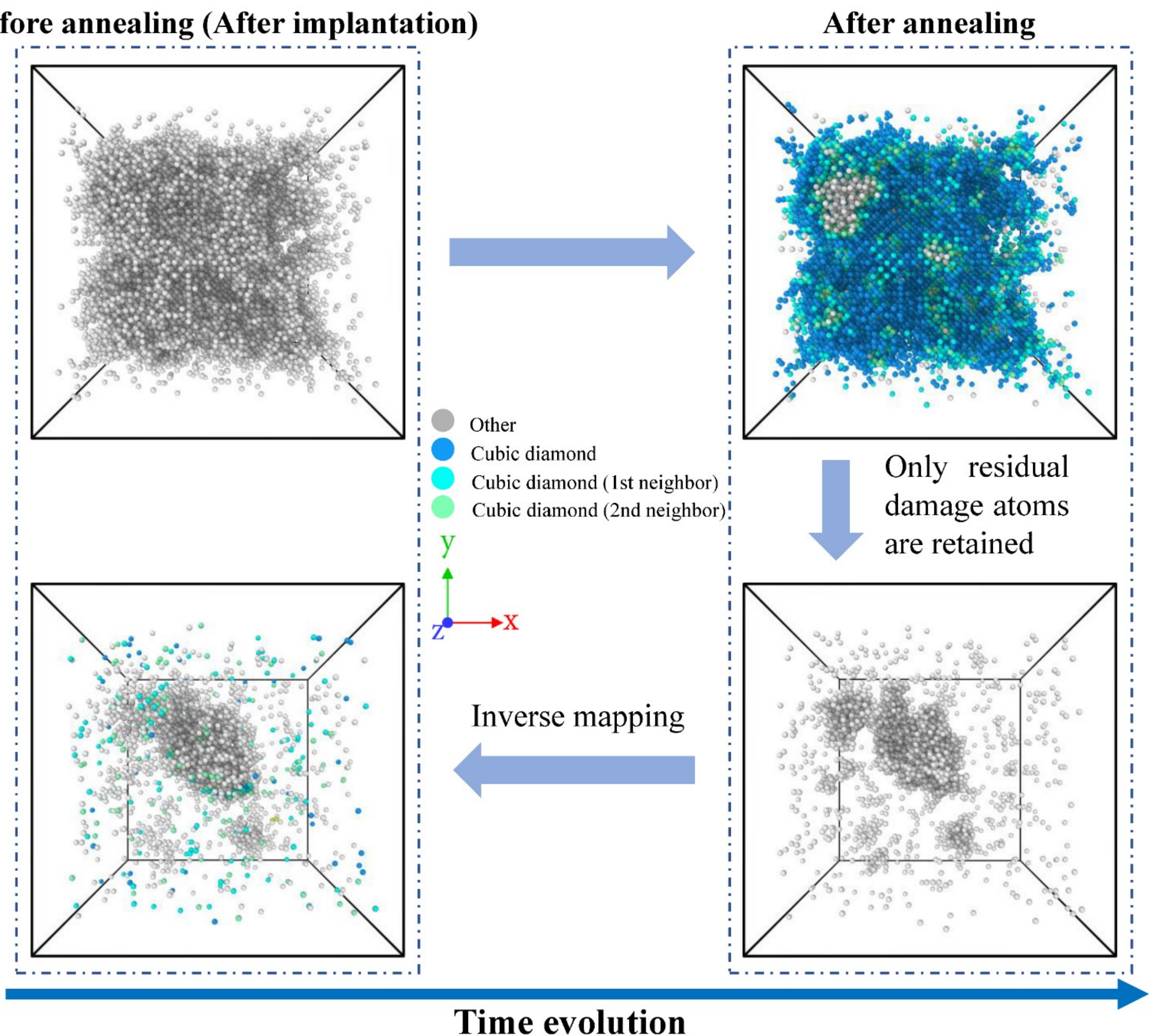

Supplementary Figure 8. Inverse mapping method to uncover annealing-induced defects (the legend selects the case of 1973 K implantation under the dose of 4.06×10^{14} cm^{-2}). The residual defect atoms after annealing are frozen, and then traced backward to the state before annealing corresponding to these certain atoms, all the CDS atoms are annealing-induced defects in this case.

Atom configuration extraction around Al atoms after annealing

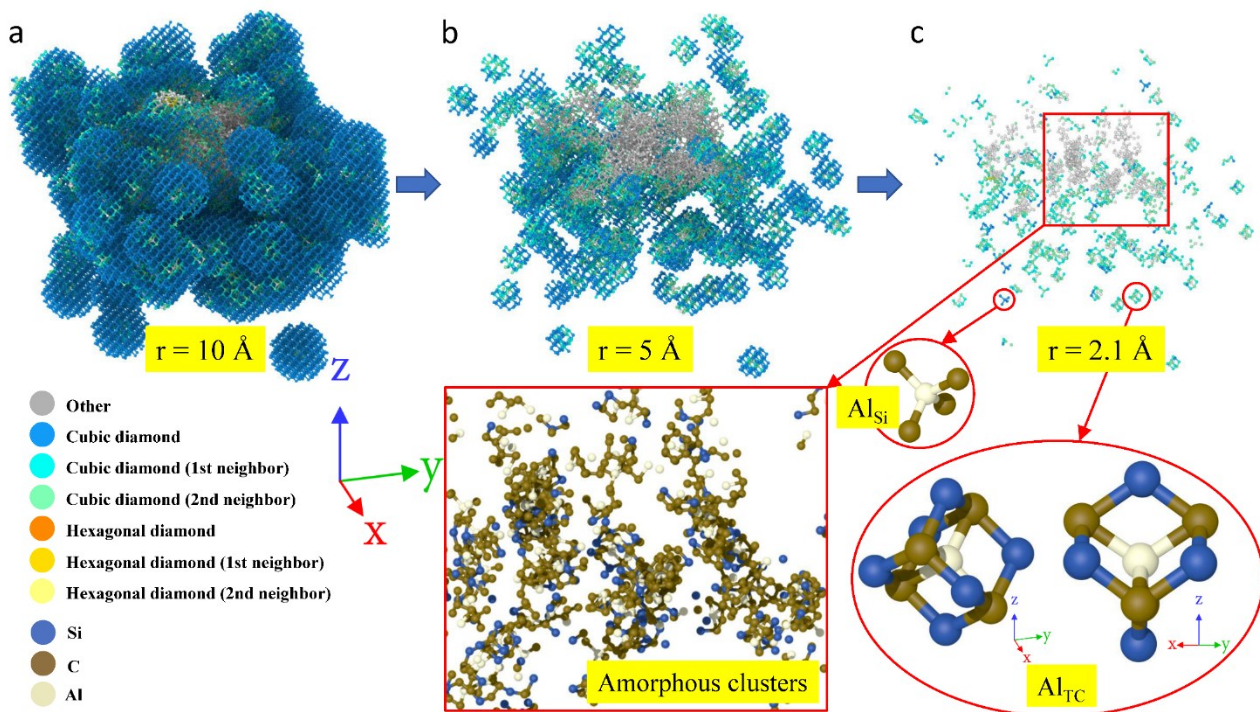

Supplementary Figure 9. The extraction of the configuration around Al atoms in different cutoff, from (**a**) to (**c**): cutoff is 10 Å, 5 Å, 2.1 Å, respectively. The legend shows after 2.35 ns annealing at 3300 K (after 1273 K implantation, implant dose: 5×10^{14} cm^{-2}). The second row shows the local details of Al and its surrounding configuration under the cutoff radius of 2.1 Å, atoms are colored according to atom type. Rectangular box shows the configuration details of the amorphous clusters in the implantation-induced damage area. Circle box shows the perfect substitutional configuration of Al. Oval box shows the most common local configuration of interstitial Al (show through two different directions).

Supplementary References

[1] G. J. Dienes, G. H. Vineyard, Radiation Effects in Solids; Interscience Publishers London Ltd: 1957.

[2] Y. Zhang, W. J.Weber, W. Jiang, A. Hallén, G. Possnert, Damage evolution and recovery on both Si and C sublattices in Al-implanted 4H–SiC studied by Rutherford backscattering spectroscopy and nuclear reaction analysis, *J. Appl. Phys*. 2002, **91**, 6388-6395.

[3] R. Spohr, Ion Tracks and Microtechnology, Principles and Applications; Vieweg, Braunschweig: 1990.

[4] X. P. Wang, M. W. Zhao, H. H Xia, S. S. Yan, and X. D. Liu, First-principles characterization of an AlSiVC center in cubic silicon carbide, *J. Appl. Phy.* 2011, **110**, 033711.

[5] J. P. Perdew, K. Burke, and M. Ernzerhof, Generalized gradient approximation made simple, *Phys. Rev. Lett.* 1996, **77**, 3865.

[6] T. Kimoto and J.A. Cooper, Fundamentals of Silicon Carbide Technology, 1st ed. (Wiley, Singapore, 2014) p. 521.

[7] Y. J. Xiao, F. Z. Fang, Z. W. Xu, X. T. Hu, Annealing recovery of nanoscale silicon surface damage caused by Ga focused ion beam, *Appl. Sur. Sci.* 2015, **343**, 56–69.